

# Giant voltage amplification from incipient ferroelectric states

Mónica Graf<sup>1</sup>, Hugo Aramberri<sup>1</sup>, Pavlo Zubko<sup>2</sup> and Jorge Íñiguez<sup>1,3</sup>

<sup>1</sup>Materials Research and Technology Department, Luxembourg Institute of Science and Technology (LIST), Avenue des Hauts-Fourneaux 5, L-4362 Esch/Alzette, Luxembourg

<sup>2</sup>London Centre for Nanotechnology and Department of Physics and Astronomy,

University College London, 17–19 Gordon Street, WC1H 0HA London, United Kingdom

<sup>3</sup>Department of Physics and Materials Science, University of Luxembourg, Rue du Brill 41, L-4422 Belvaux, Luxembourg

Ferroelectrics subject to suitable electric boundary conditions present a steady negative capacitance response. When the ferroelectric is in a heterostructure, this behavior yields a voltage amplification in the other elements, which experience a potential difference larger than the one applied, holding promise for low-power electronics. So far research has focused on verifying this effect and little is known about how to optimize it. Here we describe an electrostatic theory of ferroelectric/dielectric superlattices, convenient model systems, and show the relationship between the negative permittivity of the ferroelectric layers and the voltage amplification in the dielectric ones. Then, we run simulations of PbTiO<sub>3</sub>/SrTiO<sub>3</sub> superlattices to reveal the factors most strongly affecting the amplification. In particular, we find that giant effects (up to 10-fold increases) can be obtained when PbTiO<sub>3</sub> is brought close to the so-called “incipient ferroelectric” state.

Since its revival in 2008<sup>1</sup>, the negative capacitance (NC) response of ferroelectrics has been a focus of attention. In principle, all materials must present a positive global capacitance or dielectric constant, a necessary condition for thermodynamic stability. Nevertheless, local NC states can be obtained in a variety of ways<sup>2</sup>. Most interestingly, by placing a ferroelectric in contact with a dielectric, we can prevent it from reaching its lowest-energy state (homogenous polarization), forcing it to display a different order of relatively high energy. Such a frustrated ferroelectric will typically display a steady NC response upon application of an electric field<sup>2–4</sup>. This has been shown in detail for ferroelectric/dielectric superlattices that have emerged as model systems in the field<sup>5–8</sup>.

To understand steady-state NC, let us consider the superlattice in Fig. 1, where ferroelectric (f) and dielectric (d) layers repeat periodically along the stacking direction  $z$ . In the absence of free carriers, the continuity of the  $z$  component of the displacement vector implies  $D = D_f = D_d$ , where  $D$  is the superlattice displacement while  $D_f$  and  $D_d$  are the layer vectors (we omit the  $z$  subscript for simplicity). Using the definitions in Fig. 1, this yields

$$P + \epsilon_0 \mathcal{E}_{\text{ext}} = P_f + \epsilon_0 \mathcal{E}_f = P_d + \epsilon_0 \mathcal{E}_d, \quad (1)$$

where  $\epsilon_0$  is vacuum permittivity,  $P = L^{-1}(l_f P_f + l_d P_d)$  is

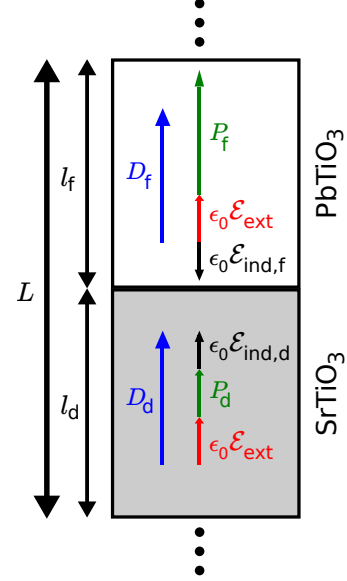


FIG. 1: Sketch of a ferroelectric/paraelectric superlattice periodically repeated along the stacking direction. The thickness of the ferroelectric and dielectric layer is given by  $l_f$  and  $l_d$ , respectively;  $L = l_f + l_d$  is the thickness of the repeated unit. For an arbitrary external field  $\mathcal{E}_{\text{ext}}$ , and in the absence of free carriers, all layers present the same vertical component of the displacement vector, so that  $D_f = D_d$ . As illustrated in the figure, the displacement  $D_i$  of layer  $i$  involves the layer polarization  $P_i$ , the field  $\mathcal{E}_{\text{ind},i}$  induced in the layer and the external field  $\mathcal{E}_{\text{ext}}$ .

the superlattice polarization,  $\mathcal{E}_{\text{ext}}$  is the external electric field along  $z$ , and the total field in layer  $i$  ( $i = f, d$ ) is

$$\mathcal{E}_i = \mathcal{E}_{\text{ext}} + \mathcal{E}_{\text{ind},i}. \quad (2)$$

Further, since  $D = D_i$  we can write

$$\mathcal{E}_{\text{ind},i} = \epsilon_0^{-1} (P - P_i), \quad (3)$$

which shows that induced fields  $\mathcal{E}_{\text{ind},i}$  appear when the local and global polarizations differ. For the f-layer we typically have  $P_f > P$ , so that  $\mathcal{E}_{\text{ind},f}$  opposes  $P_f$ ; this is the so-called “depolarizing field”.

Because of the superlattice periodicity, the total voltage associated to the induced fields must be null, which implies  $l_d \mathcal{E}_{\text{ind},d} + l_f \mathcal{E}_{\text{ind},f} = 0$ . This means that there is no net depolarizing field,  $\mathcal{E}_{\text{ext}}$  being the only macroscopic field acting on the system.

To examine the response to a variation of the external field  $d\mathcal{E}_{\text{ext}}$ , it is useful to introduce a quantity we call the “screening factor”, defined for the f-layer as

$$\varphi_f = \frac{d\mathcal{E}_{\text{ind},f}}{d\mathcal{E}_{\text{ext}}} = \epsilon_0^{-1} \frac{d(P - P_f)}{d\mathcal{E}_{\text{ext}}} = \frac{l_d}{L} (\chi'_d - \chi'_f). \quad (4)$$

Here we use the primed susceptibilities  $\epsilon_0 \chi'_i = dP_i/d\mathcal{E}_{\text{ext}}$ , which are all but guaranteed to be positive. (The change in polarization – local or global – will always follow the change in the external field. By contrast, the usual susceptibility of the f-layer  $\epsilon_0 \chi_f = dP_f/d\mathcal{E}_f$  involves the local field, and becomes negative in the NC regime.) The inverse permittivity of the f-layer can then be written as

$$\epsilon_f^{-1} = \frac{d\mathcal{E}_f}{dD} = \frac{d\mathcal{E}_{\text{ext}}}{dD} (1 + \varphi_f) = \epsilon^{-1} (1 + \varphi_f). \quad (5)$$

Further, as detailed in Supplementary Note 1, we can derive the voltage response of the dielectric layer  $\mathcal{A}_d$  as

$$\mathcal{A}_d = \frac{dV_d}{dV} = \frac{l_d}{L} \frac{d\mathcal{E}_d}{d\mathcal{E}_{\text{ext}}} = L^{-1} (l_d - l_f \varphi_f). \quad (6)$$

Voltage amplification (VA) corresponds to  $\mathcal{A}_d > 1$ . This key quantity is fully determined by trivial geometric elements and the screening factor of the f-layer.

We now use these equations to discuss the dielectric response of a superlattice. Typically the ferroelectric layers will be more responsive than the dielectric ones, so that  $\chi'_f > \chi'_d$ . From Eq. (3) we get that the induced depolarizing field  $d\mathcal{E}_{\text{ind},f}$  will oppose  $d\mathcal{E}_{\text{ext}}$ , and hence  $\varphi_f < 0$ . One usually expects the induced field to be smaller in magnitude than the applied one, so that  $-1 < \varphi_f < 0$ . It follows that  $\epsilon_f^{-1} > 0$  and  $\mathcal{A}_d < 1$ , a behavior we may call normal.

Imagine we make the ferroelectric more responsive, e.g., by varying its temperature to approach a Curie point. Then, we can eventually reach a situation where the induced  $d\mathcal{E}_{\text{ind},f}$  compensates the applied  $d\mathcal{E}_{\text{ext}}$  ( $\varphi_f = -1$ ), and the voltage drops exclusively in the dielectric layers ( $\mathcal{A}_d = 1$ ). The ferroelectric effectively behaves as a metal, and we call this “perfect screening”.

If we keep softening the f-layer so that  $\chi'_f \gg \chi'_d$ , we access a regime where the ferroelectric “over-screens”: its response is so strong that the induced depolarizing field exceeds the applied one ( $\varphi_f < -1$ ). This yields NC ( $\epsilon_f^{-1} < 0$ ) and VA in the dielectric ( $\mathcal{A}_d > 1$ ).

The above formulas show that NC and VA can be obtained from the layer polarizations, easily accessible from atomistic simulations. The so-called “second-principles” methods<sup>9,10</sup> (see Methods) have been key to explain NC in PbTiO<sub>3</sub>/SrTiO<sub>3</sub> (PTO/STO) superlattices. Here we use said methods to monitor the dependence of NC and VA on the design variables offered by these artificial materials (layer thickness, epitaxial strain), unveiling a distinct strategy to obtain giant effects.

We study PTO/STO superlattices where the PTO and STO layers have a thickness of  $n$  and  $m$  perovskite cells, respectively, denoted  $n/m$  in the following. We consider

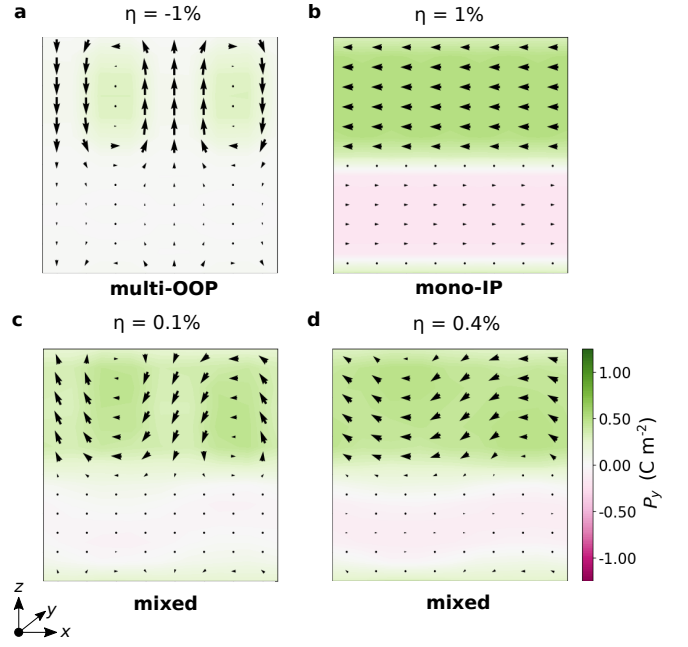


FIG. 2: Representative states found for 6/6 superlattices. Multi-OOP state for  $\eta = -1\%$  shown in panel **a**, mono-IP state for  $\eta = 1\%$  in panel **b**, and mixed states for  $\eta = 0.1\%$  and  $0.4\%$  in panels **c** and **d**, respectively. Arrows represent local polarization in the  $xz$  plane and the color scale corresponds to the polarization along  $y$ .

$n$  and  $m$  from 3 to 9, and investigate the response to small external fields along  $z$ . We also vary the epitaxial strain  $\eta$  between  $-1\%$  to  $+3\%$ , choosing the STO substrate as the zero of strain.

For computational feasibility we restrict ourselves to low temperatures (formally, 0 K) and work with periodically-repeated supercells that are relatively small in plane ( $8 \times 8$  perovskite units). As argued below, this suffices to draw conclusions on the behavior of real materials at ambient conditions.

Let us first recall the main effect epitaxial strain has on PTO/STO superlattices, as obtained from our simulations. Figure 2a shows the ground state of the 6/6 system for  $\eta = -1\%$ : it presents stripe domains in the PTO layer, with local polarizations along the out of plane (OOP)  $z$  direction. This “multi-OOP” vortex-like state has been thoroughly studied in the literature<sup>5,11–15</sup>.

For large enough tensile strains, we find the PTO layer displays a monodomain state with in-plane (IP) polarization (Fig. 2b). This simulated “mono-IP” configuration is characterized by  $P_x = P_y$ . In reality<sup>16</sup> one typically observes the so-called  $a_1/a_2$  multidomain configuration, with local polarizations alternating between  $P_x$  and  $P_y$ . Our monodomain result is a consequence of the relatively small size of the simulation supercell.

Finally, Figs. 2c and 2d show states we find in some superlattices at intermediate  $\eta$  values, where mono-IP and multi-OOP features “mix”, reminiscent of similar

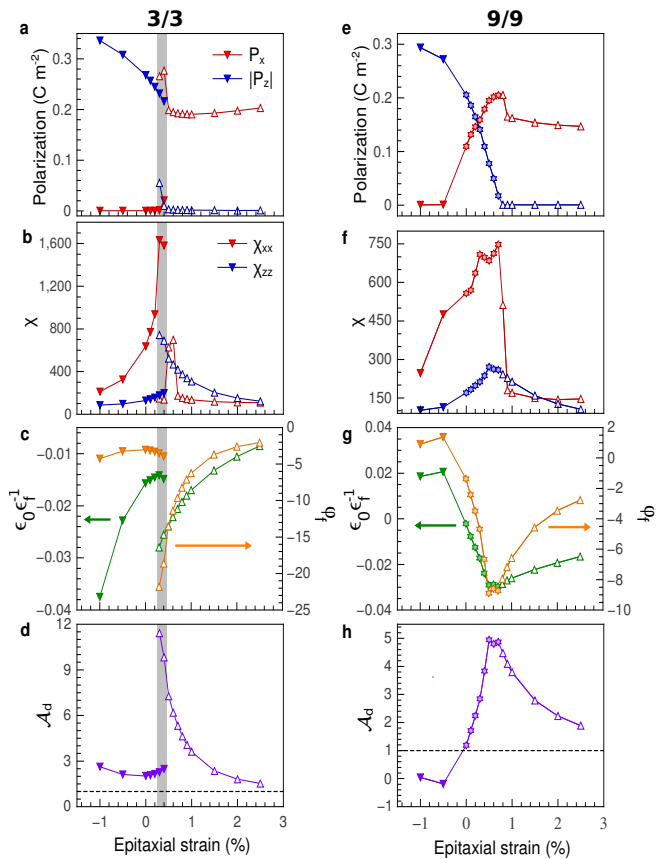


FIG. 3: Simulation results for the 3/3 (from **a** to **d**) and 9/9 (from **e** to **h**) superlattices, as a function of epitaxial strain. Panels **a** and **e** show two superlattice averages of the polarization:  $|P_z|$  corresponds to averaging the absolute value of the  $z$ -component of the local polarizations, so as to get a non-zero result in the multi-OOP state;  $P_x$  is the direct supercell average of the  $x$ -component of the local polarizations, where  $x$  is the modulation direction (perpendicular to the domain walls) in the multi-OOP and mixed states. Panels **c** and **g** show the inverse permittivity  $\epsilon_f^{-1}$  in units of  $\epsilon_0^{-1}$  (left axis) and screening factor  $\varphi_f$  (right axis) of the ferroelectric layer. Panels **d** and **h** show the voltage ratio  $\mathcal{A}_d$  of the dielectric. The gray zone in panels **a-d** marks the region where both multi-OOP and mono-IP states are (meta)stable. Dark-colored down-pointing triangles correspond to multi-OOP states, while we use light-colored stars for mixed states and empty up-looking triangles for mono-IP states.

findings in the literature<sup>15,16</sup>. In conclusion, apart from some non-essential size effects, our simulations capture the evolution of PTO/STO superlattices with epitaxial strain.

Figures **3a-d** show detailed results for the 3/3 system. At compressive and slightly tensile strains, we get a multi-OOP solution similar to that of Fig. **2a**, with  $|P_z| \neq 0$  and  $P_x = 0$ . As  $\eta$  increases, we see an abrupt transition to the mono-IP phase with  $|P_z| = 0$  and  $P_x \neq 0$ . As typical of discontinuous transformations, the multi-OOP and mono-IP states are both stable for

intermediate strains (gray area in the figure).

The global dielectric susceptibility is shown in Fig. **3b**. As we increase  $\eta$  in the multi-OOP state, we induce a maximum of  $\chi_{xx}$ , signaling the occurrence of an IP polar instability. In the case of the mono-IP state, it is  $\chi_{zz}$  that peaks as  $\eta$  decreases, indicating a soft OOP polar mode. The mono-IP state also displays a peak in  $\chi_{xx}$  at  $\eta \approx 0.6$  %; this feature, associated to the STO layer and not essential here, is discussed in Supplementary Note 2 and Supplementary Figure 1.

Figure **3c** shows the inverse permittivity (green) and screening factor (orange) of the f-layer. For all considered strains we get  $\epsilon_f^{-1} < 0$  and the associated over-screening ( $\varphi_f < -1$ ). Further, Fig. **3d** shows the corresponding VA in the d-layer, with  $\mathcal{A}_d$  reaching values as high as 12 when the mono-IP state approaches its stability limit. This giant amplification is related to the maximum in  $\chi_{zz}$  (panel **b**), in turn connected to the OOP polar instability of the PTO layer. In contrast, the destabilization of the multi-OOP state upon increasing  $\eta$  – which involves a  $\chi_{xx}$  anomaly – does not result in any feature in  $\epsilon_f^{-1}$  or  $\mathcal{A}_d$ .

As shown in Figs. **3e-h**, the 9/9 superlattice presents a similar behavior, the main difference being that we find no  $\eta$  values where two states can exist. Instead, for  $\eta$  between 0.0 % and 0.8 % we see a gradual transformation from multi-OOP to mono-IP, with the occurrence of the mixed state mentioned above (Figs. **2c** and **2d**). The small jump in  $P_x$  around  $\eta = 0.9$  % is related to the occurrence of an IP polarization in the STO layer (not relevant here; see Supplementary Note 2 and Supplementary Figure 2).

The 9/9 superlattice displays its largest NC response in this intermediate region, reaching 5-fold amplifications at the transition point between the mono-IP and mixed states. The VA extends into the mono-IP region.

In contrast, the multi-OOP state of the 9/9 superlattices shows a different behavior: see e.g.  $\mathcal{A}_d < 0$  at  $\eta = -0.5$  % in Fig. **3h**. In this regime, the PTO layer is in a very stable (stiff) multidomain configuration, while the in-plane compression makes STO electrically soft along  $z$ . Hence, the roles reverse and the STO layer displays NC. (See Supplementary Note 3 for more.) A similar behavior has been predicted in BaTiO<sub>3</sub>/SrTiO<sub>3</sub> superlattices<sup>17</sup>.

We run the same study for a large collection of superlattices; Figure 4 summarizes our results.

We find that the transition region between the multi-OOP and mono-IP states becomes wider for thicker PTO. This reflects the fact that broader PTO layers can accommodate more complex dipole orders, as the one occurring in the mixed state. (This is consistent with recent results in the literature, e.g. the occurrence of supercrystals in PbTiO<sub>3</sub>/SrRuO<sub>3</sub> superlattices with PTO layers above 15 cells<sup>18</sup>.)

The mixed state is also favored by thicker STO layers. This effect is more subtle, and probably related to the fact that the stray fields are expelled from the STO layer as it thickens. This aspect is not essential here and we

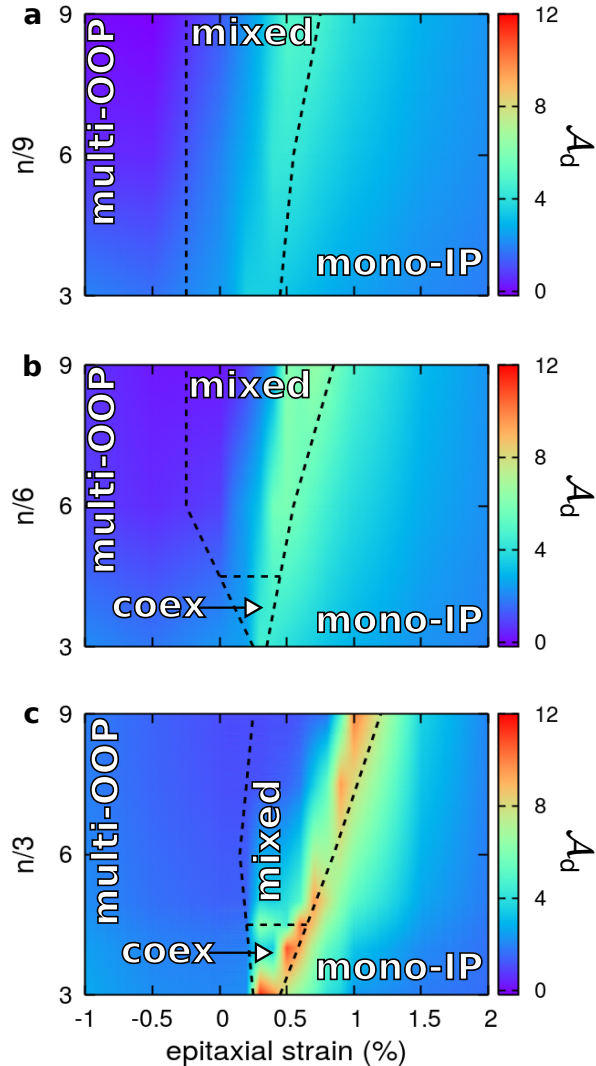


FIG. 4: Summary of our results for VA in  $n/m$  superlattices. Panels **a**, **b** and **c** present results for  $m = 3$ ,  $m = 6$  and  $m = 9$ , respectively. The color scale represents the voltage ratio  $\mathcal{A}_d$ . The lines and labels indicate the stability regions of the states of Fig. 2. In the coexistence region we show the  $\mathcal{A}_d$  values corresponding to the mono-IP state.

do not pursue it.

Most importantly, Fig. 4 confirms that the strongest amplifications occur at the stability limit of the mono-IP state. It also shows that the multi-OOP region is comparatively unresponsive. Let us now get insight into the physical underpinnings of these behaviors.

As captured by Eqs. 4 and 6, VA is essentially determined by the screening factor of the f-layer, which in turn depends on the difference in dielectric response between layers. For example, for the 3/3 superlattice at  $\eta = 0.3\%$  we get  $\mathcal{A}_d \approx 12$ , with  $\chi'_f = 765$  and  $\chi'_d = 721$ . This  $\chi'_f$  value may seem small; indeed, the ferroelectric is close to developing an OOP polar instability and, in such

conditions, one expects susceptibilities  $\chi_f > 10,000$ <sup>19,20</sup>. By contrast, the computed  $\chi'_d$  is surprisingly large, as our model for STO yields  $\chi = 202$  for the pure material. (Our simulated STO is relatively stiff as compared to experiment<sup>5</sup>; not essential here.)

The reason for these surprising  $\chi'_i$  susceptibilities can be traced back to the electrostatic requirement that  $D_f = D_d$ . This leads all layers to respond similarly to an external field, to minimize the depolarizing fields. Thus, we expect  $\chi'_f \gtrsim \chi'_d$ . For example, for the 6/6 superlattice at  $\eta = -1\%$ , which does not display VA, we obtain  $\chi'_f = 96$  and  $\chi'_d = 95$  (Supplementary Figure 3). Then, when we move to a region of the phase diagram where the f-layer presents an OOP instability, the energy gain associated to the development of  $dP_f$  overwhelms the cost of creating a depolarizing field. Hence, the difference between  $\chi'_f$  and  $\chi'_d$  grows a little, which suffices to yield large VA values.

The largest amplifications correspond to the region marking the limit of stability of the mono-IP state. We can say that, in this area, the f-layers are in an “incipient ferroelectric” state<sup>2,17</sup>: they are unstable against the development of an homogeneous OOP polarization whose occurrence is precluded by the presence of the d-layers. Eventually, as we move towards negative  $\eta$  values, the multi-OOP polar instability freezes in, leading to either a pure multi-OOP state or a mixed state, and progressively hardening the  $z$ -polarized ferroelectric soft mode. (This resembles the competition between antipolar and polar orders in antiferroelectrics<sup>21,22</sup>.) This incipient ferroelectric state corresponds to the idealized picture of monodomain NC<sup>1,2</sup>; our results predict a realization of this archetype.

As shown in Fig. 5a and already reported<sup>5,6</sup>, the NC response of multi-OOP states mainly stems from the large dielectric response (large  $\chi'$ ) of the domain walls. By contrast, in the incipient ferroelectric state the NC response comes from the full volume of the f-layer (Fig. 5b). This partly explains the superior VA performance of the mono-IP state.

Our results suggest a strategy to obtain large VA: work with incipient ferroelectric states that will typically occur at the boundary between IP and OOP phases. Phase boundaries akin to the ones discussed here have been found experimentally in PTO/STO superlattices<sup>16</sup> and predicted in other ferroelectric/dielectric heterostructures<sup>17</sup>; those are clear candidates to display giant VA effects. Note that, despite their limitations (low temperature, small supercells), our simulations capture the main physics of the IP-to-OOP transition; thus, our conclusions can be expected to apply to experimentally relevant situations.

Additionally, our electrostatic formulas teach us that  $\mathcal{A}_d$  does not depend on the macroscopic permittivity  $\epsilon^{-1}$  (Eq. 6), while  $\epsilon_f^{-1}$  does (Eq. 5). As a consequence, one can have behaviors as that of the 3/3 system at  $\eta = -1\%$  (Fig. 3): we get a very negative  $\epsilon_f^{-1}$  (panel c) not accompanied by a large  $\mathcal{A}_d$  (panel d). The reason is that this

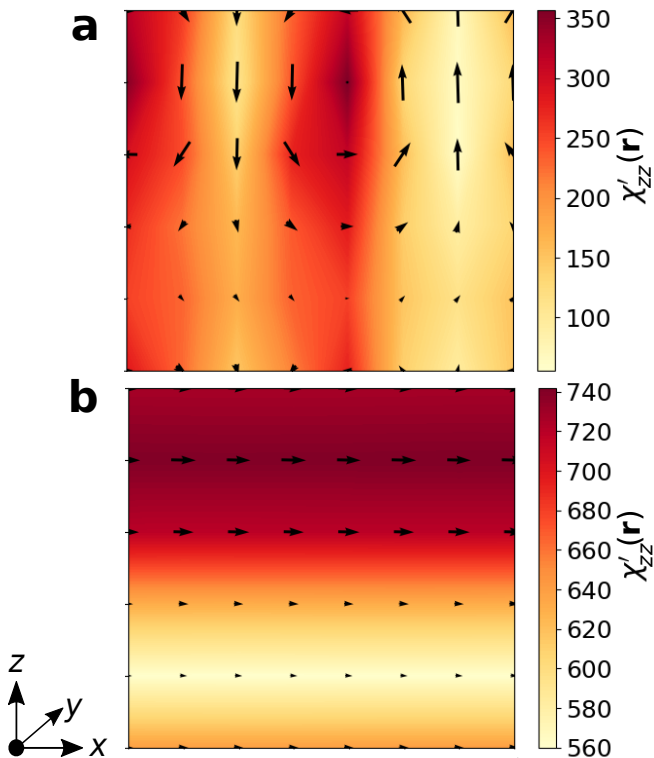


FIG. 5: Maps of the local dielectric response  $\chi'_{zz}(\mathbf{r}) = \epsilon_0^{-1} \partial P(\mathbf{r}) / \partial \mathcal{E}_{\text{ext}}$ , where  $P(\mathbf{r})$  is the position dependent  $z$ -component of the polarization and the applied field is also along  $z$ . The results correspond to a particular  $xz$  plane of the 3/3 superlattice at  $\eta = 0.4\%$ . (These structures are periodic along  $y$ .) The arrows represent the local electric dipoles in the  $xz$  plane at zero field. The shown multi-OOP (a) and mono-IP (b) states are both stable for this value of  $\eta$ . Note that the color scales differ between panels.

superlattice presents a small  $\chi_{zz}$  (panel b), which yields large  $\epsilon^{-1}$  and  $|\epsilon_f^{-1}|$ . By the same token, having a globally soft superlattice may result in a modest NC response of the f-layer, but this does not necessarily imply a small VA. Hence, there is no reason to disregard – for VA purposes – very responsive systems where small values of  $\epsilon^{-1}$  and  $|\epsilon_f^{-1}|$  have been measured or computed<sup>5–7</sup>. Rather, we must focus on the response difference between ferroelectric and dielectric layers, as captured by the screening factor  $\varphi_f$ .

Finally, let us stress that our conclusions for an ide-

alized superlattice apply to other materials too. First, note that an infinite superlattice is equivalent to a ferroelectric/dielectric bilayer contacted with good electrodes, so there is no net depolarizing field. Second, NC is perfectly compatible with non-ideal electrodes and depolarizing fields<sup>4</sup>; in fact, these fields reflect the electrostatic frustration at its origin. Hence, we expect our conclusions to apply to real systems where the development of an homogeneous polar state is precluded, including field-effect transistors featuring a ferroelectric/semiconductor bilayer.

We hope this work will bring an impetus to the study of negative capacitance, shifting the focus to the quantification and optimization of voltage amplification.

### Methods

The second-principles simulations are performed using the SCALE-UP package<sup>9,10</sup> and the same approach as previous studies of PTO/STO superlattices<sup>5,14,23</sup>. The superlattice models are based on potentials for the pure bulk compounds – fitted to first-principles results<sup>9</sup> – and adjusted for the superlattices as described in Ref. 5.

We study a collection of  $n/m$  superlattices with layer thicknesses  $n, m = \{3, 6, 9\}$ . Further, we consider an isotropic epitaxial strain  $\eta$  between  $-1\%$  and  $3\%$ , where the STO square substrate (with lattice constant of  $3.901 \text{ \AA}$ ) is taken as the zero of strain.

We work with a simulation supercell that contains  $8 \times 8$  perovskite unit cells in the  $xy$  plane (perpendicular to the stacking direction). In the  $z$  direction, only 1 superlattice period is considered. Periodic boundary conditions are assumed.

In order to find the lowest-energy state of an  $n/m$  superlattice at a given  $\eta$  and electric field value, we relax the atomic structure by performing Monte Carlo (MC) simulated annealings. During the annealings, all atomic positions and strains are allowed to vary, except for the in-plane strains imposed by the substrate. From the resulting atomic structures, we compute local electric dipoles within a linear approximation (i.e., we consider the atomic displacements with respect to the high-symmetry reference structure and multiply them by their corresponding Born charge tensors), as customarily done in second-principles studies<sup>5,23</sup>.

To compute responses, a small external field of  $0.2 \text{ MV cm}^{-1}$  is considered. We checked that this field is small enough to obtain susceptibilities and the other relevant quantities within a linear approximation.

<sup>1</sup> S. Salahuddin and S. Datta, *Nano Letters* **8**, 405 (2008).

<sup>2</sup> J. Íñiguez, P. Zubko, I. Luk'yanchuk, and A. Cano, *Nature Reviews Materials* **4**, 243 (2019).

<sup>3</sup> A. M. Bratkovsky and A. P. Levanyuk, *Phys. Rev. B* **63**, 132103 (2001).

<sup>4</sup> A. M. Bratkovsky and A. P. Levanyuk, *Appl. Phys. Lett.* **89**, 253108 (2006).

<sup>5</sup> P. Zubko, J. C. Wojdeł, M. Hadjimichael, S. Fernandez-Pena, A. Sené, I. Luk'yanchuk, J. Triscone, and J. Íñiguez, *Nature* **534**, 524 (2016).

<sup>6</sup> A. K. Yadav, K. X. Nguyen, Z. Hong, P. García-Fernández, P. Aguado-Puente, C. T. Nelson, S. Das, B. Prasad, D. Kwon, S. Cheema, et al., *Nature* **565**, 468 (2019).

<sup>7</sup> S. Das, Z. Hong, V. A. Stoica, M. A. P. Gonçalves, Y. T. Shao, E. Parsonnet, E. J. Marksz, S. Saremi, M. R. Mc-

- Carter, A. Reynoso, et al., *Nature Materials* **20**, 194 (2021), ISSN 1476-4660.
- <sup>8</sup> M. A. Pavlenko, Y. A. Tikhonov, A. G. Razumnaya, V. M. Vinokur, and I. A. Lukyanchuk, *Nanomaterials* **12** (2022).
- <sup>9</sup> J. C. Wojdel, P. Hermet, M. P. Ljungberg, P. Ghosez, and J. Íñiguez, *Journal of Physics: Condensed Matter* **25**, 305401 (2013).
- <sup>10</sup> *SCALE-UP, an implementation of second-principles density functional theory*, <https://www.secondprinciples.unican.es/>.
- <sup>11</sup> P. Zubko, N. Stucki, C. Lichtensteiger, and J. M. Triscone, *Physical Review Letters* **104**, 187601 (2010).
- <sup>12</sup> P. Aguado-Puente and J. Junquera, *Phys. Rev. B* **85**, 184105 (2012).
- <sup>13</sup> A. K. Yadav, C. T. Nelson, S. L. Hsu, Z. Hong, J. D. Clarkson, C. M. Schlepütz, A. R. Damodaran, P. Shafer, E. Arenholz, L. R. Dedon, et al., *Nature* **530**, 198 (2016).
- <sup>14</sup> S. Das, Y. L. Tang, Z. Hong, M. Gonçalves, M. McCarter, C. Klewe, F. Nguyen, K.X. Gómez-Ortiz, P. Shafer, E. Arenholz, V. Stoica, et al., *Nature* **568**, 368 (2019).
- <sup>15</sup> J. S. Baker and D. R. Bowler, *Advanced Theory and Simulations* **3**, 2000154 (2020).
- <sup>16</sup> A. R. Damodaran, J. D. Clarkson, Z. Hong, H. Liu, A. K. Yadav, C. T. Nelson, S. L. Hsu, M. R. McCarter, K. D. Park, V. Kravtsov, et al., *Nature Materials* **16**, 1003 (2017).
- <sup>17</sup> R. Walter, S. Prosandeev, C. Paillard, and L. Bellaiche, *npj Computational Materials* **6**, 186 (2020).
- <sup>18</sup> M. Hadjimichael, Y. Li, E. Zatterin, G. A. Chahine, M. Conroy, K. Moore, E. N. O. Connell, P. Ondrejko, P. Marton, J. Hlinka, et al., *Nature Materials* **20**, 495 (2021).
- <sup>19</sup> M. E. Lines and A. M. Glass, *Principles and Applications of Ferroelectrics and Related Materials*, Oxford Classic Texts in the Physical Sciences (Clarendon Press, Oxford, 1977), ISBN 9780198507789.
- <sup>20</sup> M. Graf and J. Íñiguez, *Communications Materials* **2**, 60 (2021).
- <sup>21</sup> C. Kittel, *Phys. Rev.* **82**, 729 (1951).
- <sup>22</sup> H. Lu, S. Glinsek, P. Buragohain, E. Defay, J. Íñiguez, and A. Gruverman, *Advanced Functional Materials* **30**, 2003622 (2020).
- <sup>23</sup> M. A. Pereira Gonçalves, C. Escorihuela-Sayalero, P. García-Fernández, J. Junquera, and J. Íñiguez, *Science Advances* **5**, eaau7023 (2019).

### Acknowledgements

Work funded by the Luxembourg National Research Fund (FNR) through grants INTER/RCUK/18/12601980 (M.G, J.Í.) and FNR/C18/MS/12705883/REFOX/Gonzalez (H.A.), and by the United Kingdom's EPSRC through grant EP/S010769/1 (P.Z.).